Mesoporous Materials

How to cite: *Angew. Chem. Int. Ed.* **2022,** *61,* e202114729
International Edition: doi.org/10.1002/anie.202114729
German Edition: doi.org/10.1002/ange.202114729

Plasma-Induced Nanocrystalline Domain Engineering and Surface Passivation in Mesoporous Chalcogenide Semiconductor Thin Films

Aditya Ashok, Arya Vasanth, Tomota Nagaura, Miharu Eguchi, Nunzio Motta, Hoang-Phuong Phan, Nam-Trung Nguyen, Joseph G. Shapter, Jongbeom Na,* and Yusuke Yamauchi**

Abstract: The synthesis of highly crystalline mesoporous materials is key to realizing high-performance chemical and biological sensors and optoelectronics. However, minimizing surface oxidation and enhancing the domain size without affecting the porous nanoarchitecture are daunting challenges. Herein, we report a hybrid technique that combines bottom-up electrochemical growth with top-down plasma treatment to produce mesoporous semiconductors with large crystalline domain sizes and excellent surface passivation. By passivating unsaturated bonds without incorporating any chemical or physical layers, these films show better stability and enhancement in the optoelectronic properties of mesoporous copper telluride (CuTe) with different pore diameters. These results provide exciting opportunities for the development of long-term, stable, and high-performance mesoporous semiconductor materials for future technologies.

Introduction

Engineering nanoarchitectures and nanomorphologies offers advantageous approaches for multifunctional applications. The overall properties of these nanomaterials can be determined by their composition, crystalline phase, degree of crystallinity, morphology, and dimensions. The rational and controlled design of mesoporous materials provides an opportunity to create emergent science in nanospaces. These materials have played a critical role in the performance of various applications, such as adsorption, separation, catalysis, and energy storage.[1–4] Soft-templating is a flexible synthetic method that provides excellent control of the meso-structures in addition to the dimensions and morphologies of the mesoporous materials,[5] as compared to hard-templating[6] and template-free methods.[7] This technique utilizes amphiphilic molecules, such as block copolymers, as a template that can subsequently be removed, creating ordered mesopores with low surface contamination.[8,9] Some of our groups have pioneered innovative soft-templating techniques to produce mesoporous metals using block copolymer micelles as sacrificial templates in aqueous solutions for better control of the pore diameter.[4,5] Nonetheless, mesoporous metals have limited applications in optoelectronics owing to the absence of optical band gaps.[9–11] In this regard, optically active materials hold promise for self-sustainable photon-to-electron conversion processes to initiate photo-assisted electrochemical reactions. Mesoporous semiconductors such as wide-band gap metal oxides have emerged as potential candidates for optoelectronic and energy conversion applications in the ultraviolet (UV) range.[12–14] Functionalizing semiconductor materials to cover a broader range of the electromagnetic

[*] A. Ashok, T. Nagaura, M. Eguchi, H.-P. Phan, J. G. Shapter, J. Na, Y. Yamauchi
Australian Institute for Bioengineering and Nanotechnology (AIBN), The University of Queensland, Brisbane, Queensland 4072 (Australia)
E-mail: j.na@uq.edu.au
y.yamauchi@uq.edu.au

A. Ashok, H.-P. Phan, N.-T. Nguyen
Queensland Micro- and Nanotechnology Centre, Griffith University, Nathan, Queensland 4111 (Australia)
E-mail: h.phan@griffith.edu.au

A. Vasanth
Amrita Center for Nanosciences and Molecular Medicine, Amrita Vishwa Vidyapeetham, Kochi, Kerala 682041 (India)

N. Motta
School of Chemistry and Physics
Queensland University of Technology (QUT)
2 George Street, Brisbane, Queensland 4001 (Australia)

M. Eguchi, Y. Yamauchi
JST-ERATO Yamauchi Material Space-Tectonics Project and International Center for Materials Nanoarchitectonics (WPI-MANA), National Institute for Materials Science,
1-1 Namiki, Tsukuba, Ibaraki 305-0044 (Japan)

J. Na
Research and Development (R&D) Division, Green Energy Institute, Mokpo, Jeollanamdo 58656 (Republic of Korea)
E-mail: j.na@gei.re.kr

© 2022 The Authors. Angewandte Chemie International Edition published by Wiley-VCH GmbH. This is an open access article under the terms of the Creative Commons Attribution Non-Commercial License, which permits use, distribution and reproduction in any medium, provided the original work is properly cited and is not used for commercial purposes.

 © 2022 The Authors. Angewandte Chemie International Edition published by Wiley-VCH GmbH

spectrum, including the visible wavelength range, could potentially create new exciting applications.[15,16]

Issues with previous approaches involve serious limitations in the composition of semiconductors. . Semiconductors, such as transition metal chalcogenides, can operate efficiently in the visible spectrum with highly controllable compositions, unlike metal oxides. The introduction of mesopores into the bulk of semiconductors through the soft-template method is a low-energy process, which results in nanocrystalline domains.[5,17] As domain boundaries can impede effective charge transport within mesoporous structures, high crystallinity is desirable. Several postprocessing techniques have been employed in porous and semiconductor materials to control defect sites at the lattice level to improve carrier transport and catalytic properties.[18–20] Techniques such as wet chemical passivation and physical layers have been widely employed for surface passivation.[21,22] However, these methods typically lead to the formation of high interfacial capacitance, impeding carrier mobility. Additional post-thermal annealing has been used to overcome the above issues and minimize interfacial capacitance, but this approach raises other technical problems including distortion and collapse of nanoarchitectured voids.

Plasma, the fourth state of matter, is a promising medium comprised of different species, including ions and free radicals, engendered at ambient or low pressure, including ions and free radicals.[23] Unlike ground-state atoms, plasma species remain highly reactive and can modify nanomaterials in an energy-efficient manner. Plasma-enabled material processing includes material thinning,[24] nanostructured band gap tuning,[25] heteroatom doping,[26] and surface functionalization.[27,28] Such complex reactions cannot be achieved easily by traditional thermal or solution-based treatments, making plasma processing an extremely versatile technique.

Herein, we report a new concept of coupling our soft-templating growth method with plasma exposure to obtain highly crystalline mesoporous semiconductors. We investigated the effect of varying the pore diameter and the impact of Ar plasma exposure on the mesoporous structure of copper chalcogenide. This technique proved to be less invasive and was effective in improving the crystallinity of the electrochemically deposited thin films. Spectroscopic analysis was used to examine the effective change in the photon-matter interactions upon introducing symmetrically distributed pores with different diameters to control the tunability of the band gap (E_g). The drastic improvement in domain sizes with controlled plasma exposure resulted in significantly enhanced resilience to surface oxidation. Based on this finding, an innovative approach is proposed to control the optoelectronic properties and improve the domain size in mesoporous materials.

Results and Discussion

Electrochemical Deposition of Chalcogenide Semiconductors

This study demonstrates our plasma treatment technique for mesoporous and nonporous copper telluride (CuTe) films. Our approach can also be applied to a wide range of mesoporous semiconductors. Pristine CuTe films were electrochemically prepared in an electrolyte solution containing metal ions with and without polymeric micelles under a suitable potential to form mesoporous and nonporous films using a three-electrode electrochemical system (Figure 1). We controlled the pore diameter of the CuTe films by varying the molecular weight of the amphiphilic diblock copolymer (BCP). Self-assembled micelles were made of BCPs consisting of a hydrophobic polystyrene (PS) head anchored to a hydrophilic polyethylene oxide (PEO) tail.. To initiate the self-assembly of BCPs into micelles, the suspension with tetrahydrofuran (THF) was mixed with deionized water. Subsequently, the hydrophobic PS groups were transformed into spheres, resulting in the formation of spherical micelles (Figure 1A). We optically confirmed the presence of spherical micelles by employing the Tyndall effect, in which the scattered light was more profound as the size of the micelles increased along the path of the beam. The average micelle sizes and their distributions were observed using transmission electron microscopy (TEM) for three types of homogeneously self-assembled PS-*b*-PEO micelles (Figure S1). At a suitable applied potential, the metal ions are directed towards the Au electrode, initiating nucleation and growth by trapping micelles to form a mesopore architecture through electrochemical deposition (ECD) (Figures 1B and C; further details are available in Supporting Information Note 1). Finally, the samples were rinsed with THF at 45 °C to accelerate the removal of self-assembled micelles. The mesoporous films were prepared with BCP-1, BCP-2, and BCP-3, and these samples were noted as BCP-1 film, BCP-2 film, and BCP-3 film, respectively. The optimization of the deposition potentials and stoichiometries was conducted through linear sweep voltammetry and by controlling the ratios of the metal precursors (Figures S2 and S3).

Figures 2A–H show the morphology of CuTe films characterized using field emission scanning electron microscopy (FE-SEM) along with the subsequent atomic composition determined by energy dispersive X-ray analysis (EDX) and X-ray photoelectron spectroscopy (XPS). The nonporous and mesoporous films were relatively flat with uniformly distributed pores displayed on the mesoporous films. Further details are discussed based on the amperometric current over time (*i*–*t*) during the ECD (Figure S4 and Supporting Information Note 2). To further confirm the consistency of the flat surface and the conformal pore distribution, the deposition duration of BCP-3 film (large pores) was varied to observe its effect on the morphology (Figure S5). Evidently, the surface roughness and pore distribution remained consistent with a linear increase in the film thickness at a growth rate of ca. 0.2 $nm\,s^{-1}$. The distribution of pore size and its corresponding wall thickness

© 2022 The Authors. Angewandte Chemie International Edition published by Wiley-VCH GmbH

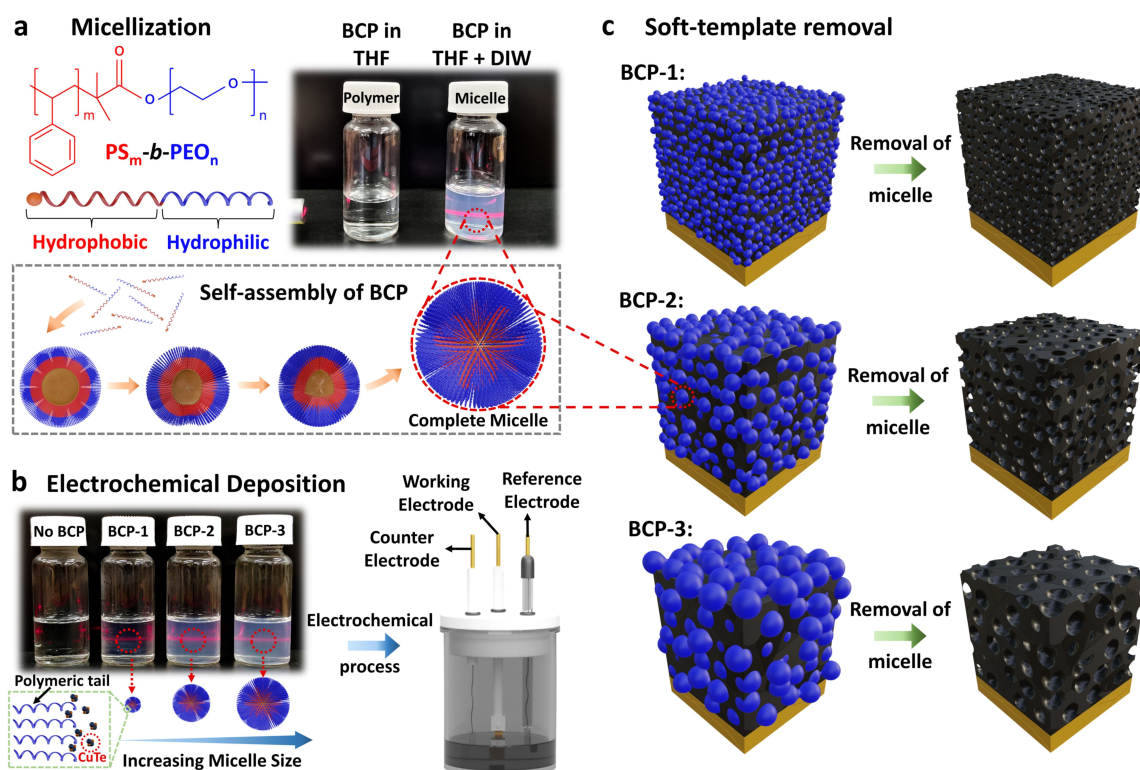

Figure 1. Illustration of the process flow for the deposition of mesoporous CuTe thin film. A) Di-block copolymer (BCP) dissolved in tetrahydrofuran (THF) and self-assembled to form micelles when introduced in deionized water (DIW). B) Electrochemical deposition process for nonporous (without BCP) and mesoporous BCP-1, BCP-2 and BCP-3 films with varying micelle sizes in the electrolyte solution. C) THF-assisted soft-template removal to obtain mesoporous films.

were extracted from the SEM images shown in Figures 2A–H. Figure 2I shows the distribution in pore diameter, where the smallest pore-sized BCP-1 film was found to be 9.4 nm and gradually increased to 16.2 nm for BCP-2 film and 20.9 nm for BCP-3 film with increasing molecular weight. The wall thicknesses of these films were measured at 9.2, 14.8 and 19.2 nm for BCP-1, BCP-2, and BCP-3 films, respectively (Figure 2J).

Figure 2K shows the optical absorbance of pristine films, namely, nonporous (NP) film, followed by mesoporous BCP-1, BCP-2, and BCP-3 films using spectrophotometry. A blue shift was clearly observed upon reducing the pore diameter, which in turn reduced the wall thickness of the deposited CuTe films. As the micelle size decreased, a large number of micelles could be accommodated in the bulk of the thin film during ECD, causing a reduction in the wall thickness. The presence of micelles during ECD resulted in the confined growth of crystallites, leading to low crystallinity, as further discussed in the grazing incidence X-ray diffraction (GIXD) section. This potentially results in a reduction in the average crystalline domain size and interplanar distance in the CuTe walls.[29] As the wall thickness decreases, the number of functional sites is expected to increase, creating higher-energy surface states. These surfaces (or band tailing states) can be observed at the optical band edges of the material, and are referred to as the Urbach energy (E_U): $\alpha = \alpha_0 e^{(h\nu/E_U)}$ where α is the absorption coefficient of the material (Figure S6).[30] From the slopes of the absorption spectra in Figure 2K (i.e., $ln(\alpha)/h\nu$), E_U is determined to be 599 meV for the pristine film and increases significantly with decreasing pore diameters in mesoporous films (i.e., 713, 842, and 900 meV for BCP-3, BCP-2, and BCP-1, respectively, Figure 2L and Table S1). A large E_U corresponds to a high level of disorder or an amorphous nature of the material, further emphasizing the importance of post-growth treatment to enhance the crystallinity of mesoporous semiconductors.

Concept of Post-Synthesis Plasma Irradiation

Pristine CuTe films were exposed to low-power plasma, and the results were benchmarked against the conventional thermal annealing method. In the thermal approach, we annealed NP, BCP-1, BCP-2, and BCP-3 films at 70, 140, and 210 °C for each set of films in vacuum. The original mesoporous structures were distorted and finally collapsed at temperatures of 140 °C and above, as observed by FE-SEM (Figure S7). A higher annealing temperature resulted in a high Cu migration rate towards the Au substrate, leaving a Te-rich layer on the top of the Au surface (Figure S8). Thermal treatment also requires a relatively long processing time, typically 60–90 min, which potentially increases surface oxidation.

© 2022 The Authors. Angewandte Chemie International Edition published by Wiley-VCH GmbH

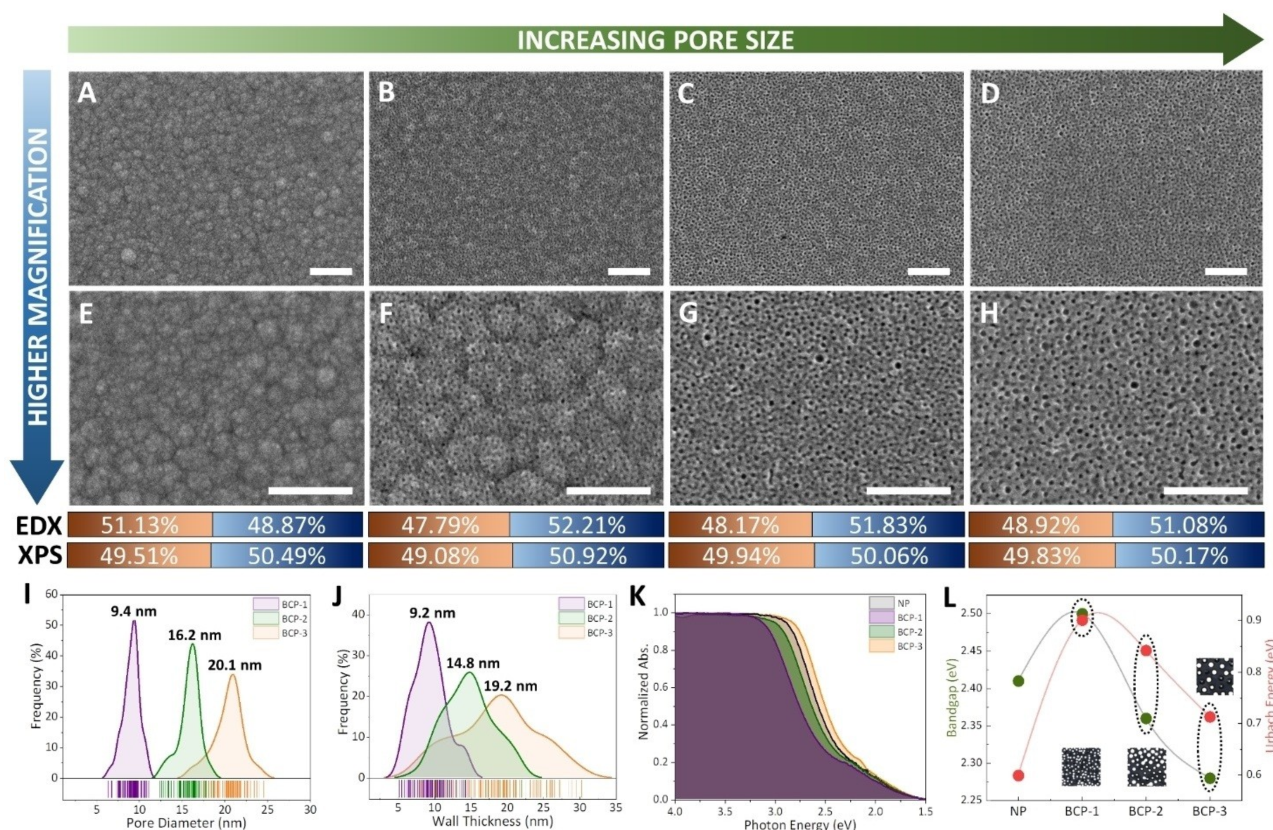

Figure 2. Scanning electron microscopy (SEM) and spectrophotometry. Surface morphologies of A, E) NP, followed by B, F) BCP-1 film, C, G) BCP-2 film, and D, H) BCP-3 film along with atomic percentages of copper in orange and telluride in blue examined by energy-dispersive X-ray analysis (EDX) and X-ray photoelectron spectroscopy (XPS) for respective samples (scale bar: 250 nm). I) Pore diameter and J) wall thickness distribution. K) Normalized absorbance along with L) band gap (E_g) and Urbach energy (E_U) for varying pore diameters. The electrolytes containing micelles were prepared by mixing 0.35 mL of 80 mM Cu precursor solution and 0.65 mL of 80 mM Te precursor solution. The applied potential was −0.2 V (vs. Ag/AgCl).

Compared to conventional annealing processes, under an optimal plasma power, chemically inert ionized gas (e.g., Ar) can passivate unsaturated surface dangling bonds without modifying the surface chemistry of materials, leaving the original nanoarchitectures unaltered under low-power plasma exposure (Figure 3). We applied low-power plasma (below 70 W) to the pristine NP and mesoporous films using radio frequency (RF) sourced at 13.56 MHz in a parallel plate configuration, as shown in Figure 3A. High-energy ions excited from the plasma are directed towards the sample, leading to elastic collisions. These elastic collisions cause the lattice to resonate and rearrange, as confirmed by the high peak intensities. The energy is then transferred in the form of momentum accompanying the anionotropy on the CuTe framework and modifies its surface energy. These low-surface-energy collisions generate localized heating through acoustic phonons at the lattice level.[23] This phenomenon is highly consistent in films with nanoscale wall thicknesses ranging from 10 to 50 nm, as ripples created in the atomic lattice due to low-energy collisions can propagate easily. During this process, the localized states extended to E_g at different energy levels are reduced by passivating the unsaturated bonds at the surface level. By varying the plasma power, the collision intensity can be tuned between elastic and inelastic collisions, resulting in different plasma-material interactions (Figure 3C). Here, we varied the plasma power and exposure time to optimize plasma parameters. Optimizing the exposure time, we ensured that Ar ion collision did not affect the nanoarchitecture, as further discussed in Figures 3B and S9, and mapped the optimization data by varying the plasma power vs. exposure time as a function of surface state passivation and domain size enhancement, for improved photon management. These results suggest that 180 s of 30 W plasma was the shortest optimal duration for the treatment of mesoporous CuTe. The effect of varying the plasma power for a fixed duration is indicated by red dots along the X-axis and varying the exposure duration for a fixed power is indicated by blue dots along the Y-axis on the graph (Figure 3B). The effect of Ar plasma on the porous structure with different powers of 10, 30, and 50 W, and the same exposure time of 180 s is presented in Figure S10. The top-view SEM images in Figures S10C and S10F confirmed that no significant change in the mesoporous structure with increasing plasma power, with a slight change in the surface roughness at 50 W, which was attributed to an etching effect, as demonstrated in Figures 3C (iv), S11, S12A, and Table S2. Furthermore, the substrate temperatures changed between 23 and 35 °C on

© 2022 The Authors. Angewandte Chemie International Edition published by Wiley-VCH GmbH

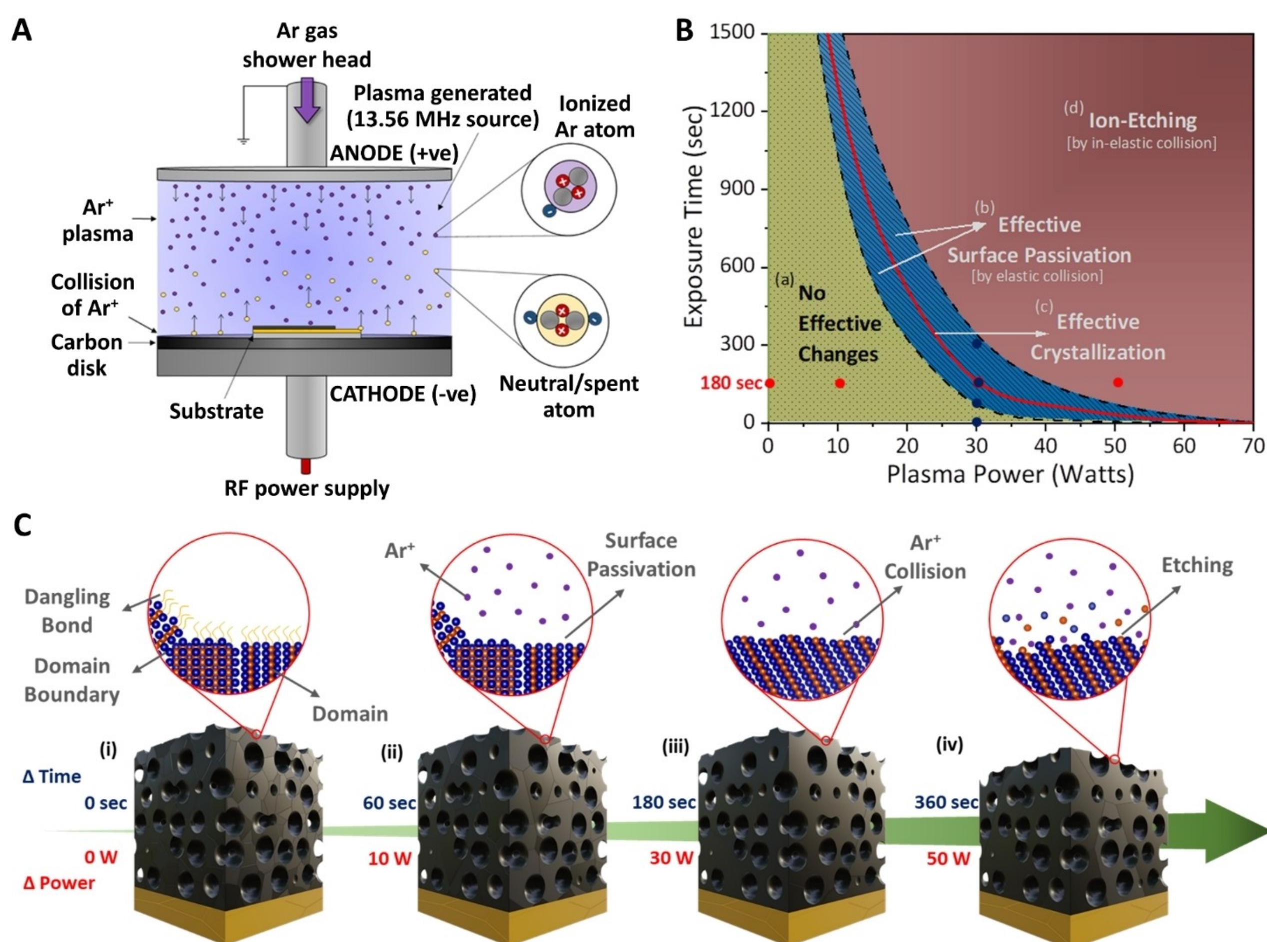

Figure 3. Plasma processing and optimization. Illustration representing A) the plasma processing chamber followed by B) process mapping from optimization and C) effect on CuTe film with change in exposure time and change in plasma power.

average, depending on the plasma power and exposure time during the Ar plasma treatment. These temperatures were measured by thermocouples sandwiched between the sample and the stage to prevent direct exposure to plasma. Because the temperatures measured in this process were similar to the ambient temperature and very low compared to the annealing temperature, the thermal effect of the low-power plasma treatment was negligible (Figure S12B).

Spectroscopic Analysis of the Plasma-Treated Films

To understand the crystallography of the material, we performed GIXD measurements in the out-of-plane configuration on films with a thickness of a few nanometers. Figures 4A and B show the GIXD patterns of the NP and mesoporous films before and after plasma treatment at 30 W for 180 s. Compared with the NP film, the GIXD patterns acquired from the pristine mesoporous films showed low-intensity widened peaks corresponding to polycrystalline frameworks (Figure 4A). As shown in Figure 2K, such broad peaks imply non-uniform strains between the micelle and the walls of CuTe on crystallization as a reinforcing mechanism.[31,32] From Figures 2I and S1D, an approximately 25 % reduction in the actual micelle size upon the growth of CuTe domains results in the formation of multiple crystalline domains around the micelles.

In contrast, plasma treatment significantly improved the domain size (Figure 4B), contributing to several distinguishable GIXD peaks with high intensity (Supporting Information Note 3). There was no significant change even under prolonged exposure to Ar plasma at 10 W (Supporting Information Note 4). Increasing the plasma power to 30 W led to a steady expansion of the crystal domains, but further improvement of the domain sizes was not observed after 180 s (Figure S13 and Table S3). Table S4 summarizes the *d*-spacing values extracted after treatment (Figure 4B) with the corresponding crystallinity (note: the *d*-spacing values for pristine films are not listed because it is difficult to extract accurate values due to very broad peaks.). Evidently, the *d*-spacing values changed slightly under the optimized plasma conditions, maintaining high consistency even when the pore diameters were varied. Regardless of the pore size, the *d*-spacings of each orientation exhibited a very slight change (Figure S14A). Furthermore, they did not change significantly depending on the plasma processing time in

© 2022 The Authors. Angewandte Chemie International Edition published by Wiley-VCH GmbH

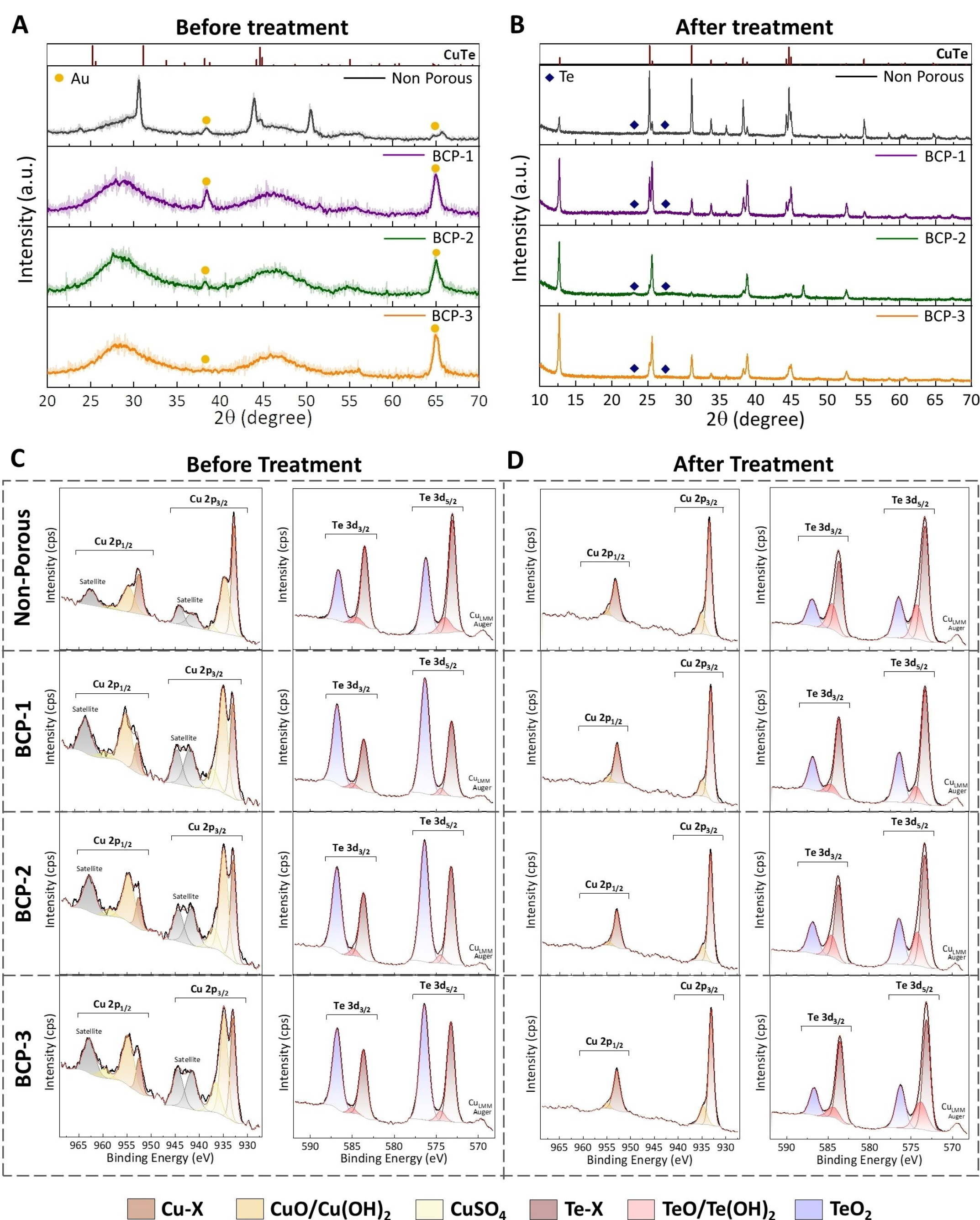

Figure 4. Grazing incidence X-ray diffraction (GIXD) and XPS on CuTe films. Out-of-plane GIXD and XPS spectra of CuTe films A, C) before and B, D) after plasma treatment under optimized conditions (30 W, 180 s).

BCP-3, which had the largest pores (Figure S14B). This phenomenon elucidated the effectiveness of optimal plasma exposure in improving the crystallinity of mesoporous materials by rearranging lattice atoms.

The optical absorption spectra of the films after thermal and plasma treatments showed no significant changes in CuTe films (Figure S15). The pristine films showed a relatively larger E_g than that of the treated films. However, a noticeable effect on the E_U was confirmed after the thermal and plasma treatments. Especially after plasma treatment, the E_U reduced with an abrupt improvement in crystallinity on increasing the exposure duration, and the *d*-spacing value also slightly reduced (30 W). Upon further exposure (above 240 s), the E_U increased along with a slight increase in *d*-spacing due to the etching of the plasma treatment (Figure S14C). According to this result, it can be confirmed that plasma treatment can control the E_U and significantly improve crystallinity with minimal changes in *d*-spacing. Further, changes in the work function and band edges (Figure S16) were extracted using ultraviolet photoelectron spectroscopy (UPS). Figure S17 shows the energy-band diagram of CuTe obtained from the energy levels. The

© 2022 The Authors. Angewandte Chemie International Edition published by Wiley-VCH GmbH

Fermi level of the samples was found to be aligned steadily at approximately 2 eV above the valence band, ensuring that the material was *n*-type even after the treatment. All the plasma treated mesoporous films maintained the same energy levels as those of the pristine films, clearly indicating the stability of the pore architecture.

To examine surface oxidation, the surface chemistry of the CuTe films was characterized using XPS with core-level spectra measured for Cu 2*p* and Te 3*d*. The peak positions and indexing are explained in Supporting Information Note 5. Figure 4C shows the core-level spectra for all pristine films. Mesopores expose many unsaturated bonds that are susceptible to ambient gas molecules, mainly oxygen, to form a thin oxide layer within a few hours of exposure. Upon further probing, it was evident that surface oxidation increased with a reduction in the pore diameter. The Cu 2*p* and Te 3*d* oxide peaks increased gradually as the pore size decreased along BCP-3 film (20.9 nm), BCP-2 film (16.2 nm), and BCP-1 film (9.4 nm). In thermally treated films, the collapsed pores trapped the surface-level oxides by chemically absorbing them into the bulk. This phenomenon was reflected in the observation of intense oxide peaks immediately after the thermal treatment. Higher annealing temperatures resulted in a high degree of surface oxidation (Figures S18A, S19A, S20A, and Supporting Information Note 5). These results indicated that post-thermal treatment was not preferable for eliminating the surface oxides. In contrast, the plasma technique showed saturation of the surface bonds, as observed in the diminution of the E_U values, as well as a significant decrease in oxide peaks (Figure 4D). Exposure to optimal plasma not only passivated the unsaturated bonds, but also eliminated the existing surface oxides and other contaminants, making the film surface resilient to oxidation. Further investigation of the long-term stability of the thermal and plasma treated films is also discussed (Figures S18–S23, Table S5, and Supporting Information Note 5).

Figures 5, S24, and S25 show cross-sectional TEM images of mesoporous CuTe used to evaluate the crystalline domain sizes and lattice arrangements. The ECD resulted in small domains (5–20 nm width) with different crystal orientations (Figures 5A–C). The fast Fourier transform (FFT) images (inset) supported the changes in domain sizes and orientations observed in the TEM images. The bright-field (BF) STEM data showed a clear improvement in the domain size of the plasma treated samples, irrespective of the varying pore diameters (Figures 5D–F), which corresponded to the crystallinity values (%) calculated from the GIXD (Figure S13 and Table S3). Along with the structural enhancement, we also observed that the domains were preferentially oriented along the vertical direction from the substrate, observed along the [010] (Figures 5G and H) or [001] zone axis (Figure 5I). The plasma sheath interacts perpendicularly with the sample surface maintained at the opposite potential by generating parallel plasma. For the orthorhombic structure of the vulcanite phase, the direction of carrier transport along the (110) plane is preferential over the *c*- axis owing to its larger *d*-spacing (6.93 Å) (Figure 5J). This directed the lattice arrangement in the walls to preferentially orient vertically from the substrate as a consequence of the shortest charge transport pathway for plasma ions (see Supporting Information Note 6). The *d*-spacing varied slightly owing to non-uniform strains (Figure S25), and the lattice fringes were coherently extended across the mesopores. Figure S26 shows the atomic resolution of CuTe along the [010] zone axis, with an overlaid orthorhombic crystal structure. Nanoscale elemental mapping after plasma treatment is further discussed in Supporting Information Note 6 using EDX analysis (Figures S27–S29). Both Cu and Te were uniformly distributed within the pore walls. Careful observation using the high-angle annular dark-field (HAADF) mode revealed segregation of several Te nanoclusters (approximately 2 nm on average) in the BCP-3 film with large pores (Figure S29), but they were not observed in the BCP-1 film with small pores (Figures S27, S28 and S30). Thus, most of the Cu and Te existed within the pore walls, whereas several Te nanoclusters were formed along the surface of the pores. Considering the 1:1 stoichiometry of CuTe, an excess amount of Te was present in the initial films (Figures 2A-H). Therefore, during plasma treatment, excess Te was knocked out from the pore walls, as identified by the Te peaks in the GIXD data (Figure 4B).

Electrical Properties of the Plasma-Treated Films

The electrical properties at the nanoscale were analyzed using a conductive atomic force microscopy (C–AFM) module to probe the effect of passivated surface states and improved the domain size (Figures 6A–H). The films were profiled by rastering the mesoporous surface at a constant amplitude using a conductive probe with a tip diameter of 15 nm. Figures 6A and E illustrate the topographies of BCP-3 films before and after plasma treatment, showing an average surface roughness (R_q) of 4.72 and 3.56 nm over a scanning area of 1 μm × 1 μm, respectively. To probe the effect of the mesopores, the contact potential difference (CPD) and the corresponding derivative electrical field difference (EFD) were measured (Figures 6B and F) by Kelvin probe force microscopy (KPFM) under an applied bias voltage scanned along the red line that crosses five pores, as indicated in Figures 6A and E. The deposition conditions were tuned to obtain a conformal thickness in the mesoporous films to minimize scattering centers and improve carrier mobility. The CPD distribution of the plasma treated film shifted to 250.9 mV higher than that of the pristine film. The CPD shift was resulted from the enhancement in the domain size accompanied by an electrically preferred orientation over the substrate. The average fluctuations in CPD (δ_{CPD}) were found to be 37.07 mV for the pristine film and 6.48 mV for the plasma treated film. Notably, the pristine film with a wide CPD distribution (Figure S31A) was attributed to a high density of defects that could lead to a high probability of carrier trapping and lower barrier voltages. Based on the one-to-one corresponding pore region indicated by the grey window across CPD and EFD, we confirmed a change in barrier voltages across the pore with an average depletion width (D_W) of 7.7 nm for

© 2022 The Authors. Angewandte Chemie International Edition published by Wiley-VCH GmbH

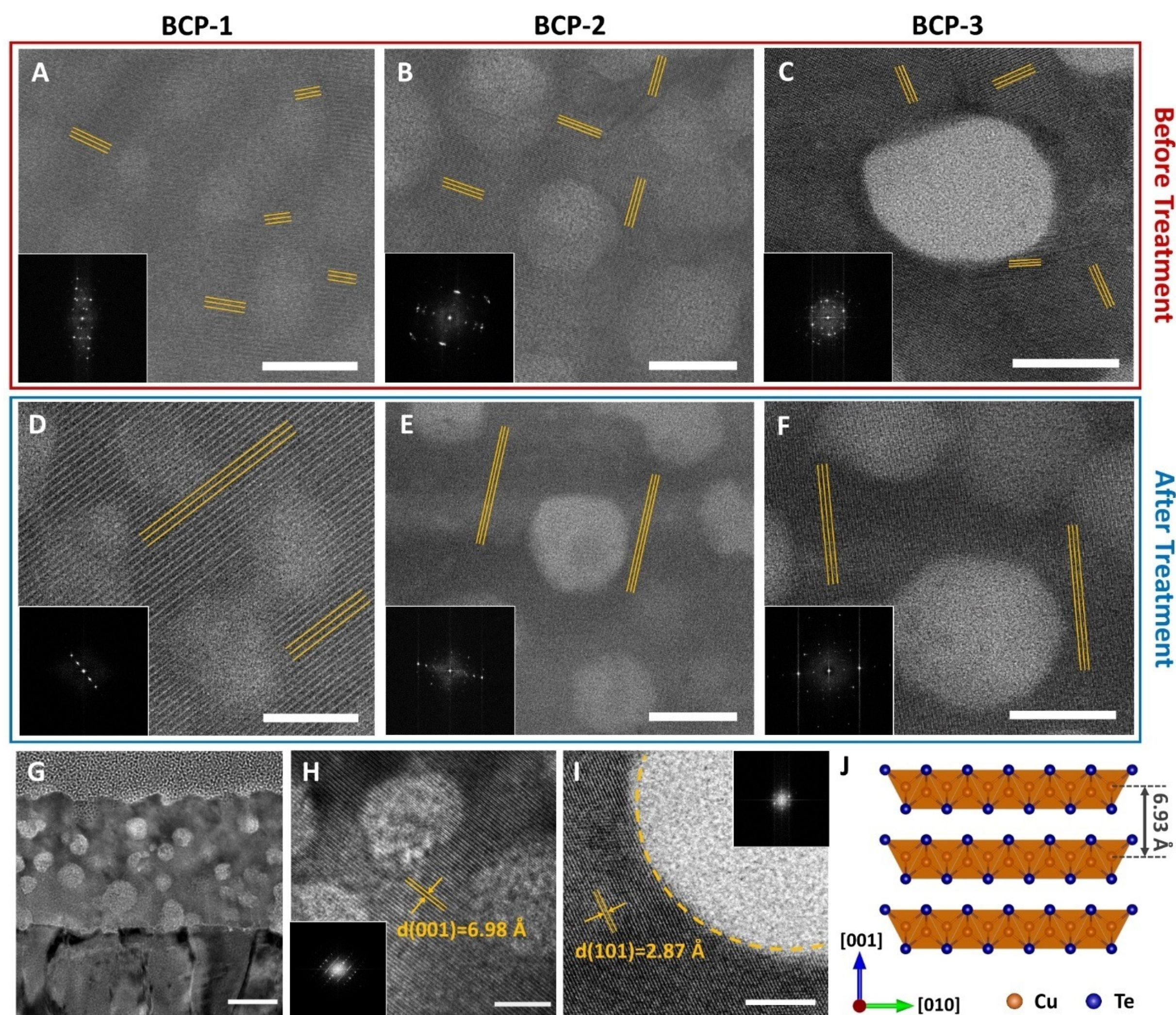

Figure 5. Transmission electron microscopy (TEM) results. Cross-sectional scanning transmission electron microscropy bright-field (STEM-BF) images of samples before and after plasma treatment: A, D) BCP-1, B, E) BCP-2, and C, F) BCP-3 films with fast Fourier transform (FFT) inset, scale bar = 15 nm. G–I) TEM images of BCP-3 film: G) cross-section, scale bar = 50 nm, H) HR-TEM along zone axis [010], scale bar = 10 nm, and I) HR-TEM along zone axis [001], scale bar = 5 nm, with corresponding FFT insets. J) Crystal structure of vulcanite phase CuTe along [100].

the pristine film. The treated film showed a wider D_W of 12.47 nm, leaving approximately no EFD along the walls of the film. This indicated that the nanoarchitecture altered the potential differences across the pore walls, where mesopores created spatial separation for charge carriers. The spatially separated carriers created along the mesopores are much lower, establishing a higher EFD as the pore size reduces, resulting in large domain boundaries in nanocrystalline materials.[22,33,34] The mobile carriers accumulated or trapped, which affected, and created a localized charge build-up at domain boundaries that acted as carrier trapping/recombination sites. The density of surface states was reduced upon exposure to plasma, making carrier transport more ballistic in the nanoscale walls. The rearranged domains with a lower R_q resulted in a 6-fold reduction in CPD fluctuations and maintained a higher charge separation or barrier width, which facilitated effective carrier collection. To understand the existence of localized states at the surface and bulk, PeakForce tunneling atomic force microscopy (PF-TUNA) under different bias conditions was carried out along with the current profile measured over the same area. The topographies of the pristine and treated films were measured at 0 and 1.3 V, as shown in Figure 6. The before- and after-treated films showed relatively better topography at zero bias (Figures 6A and E), with no observable TUNA current profiles. As the applied bias ramped-up to 1.3 V, a large number of carriers were trapped in the surface and bulk states, as indicated by the TUNA current profile. The trapped charges created a local field due to the capacitance effect, causing the probe to ripple away from the surface, resulting in a distorted surface topography for the pristine samples (Figures 6C and D). This effect persisted until the trapped carriers lost their energy completely, even when the applied bias was reduced back to 0 V (Figures S31B and S31C). These phenomena were eliminated upon energetically passivating the sample through Ar plasma, making

© 2022 The Authors. Angewandte Chemie International Edition published by Wiley-VCH GmbH

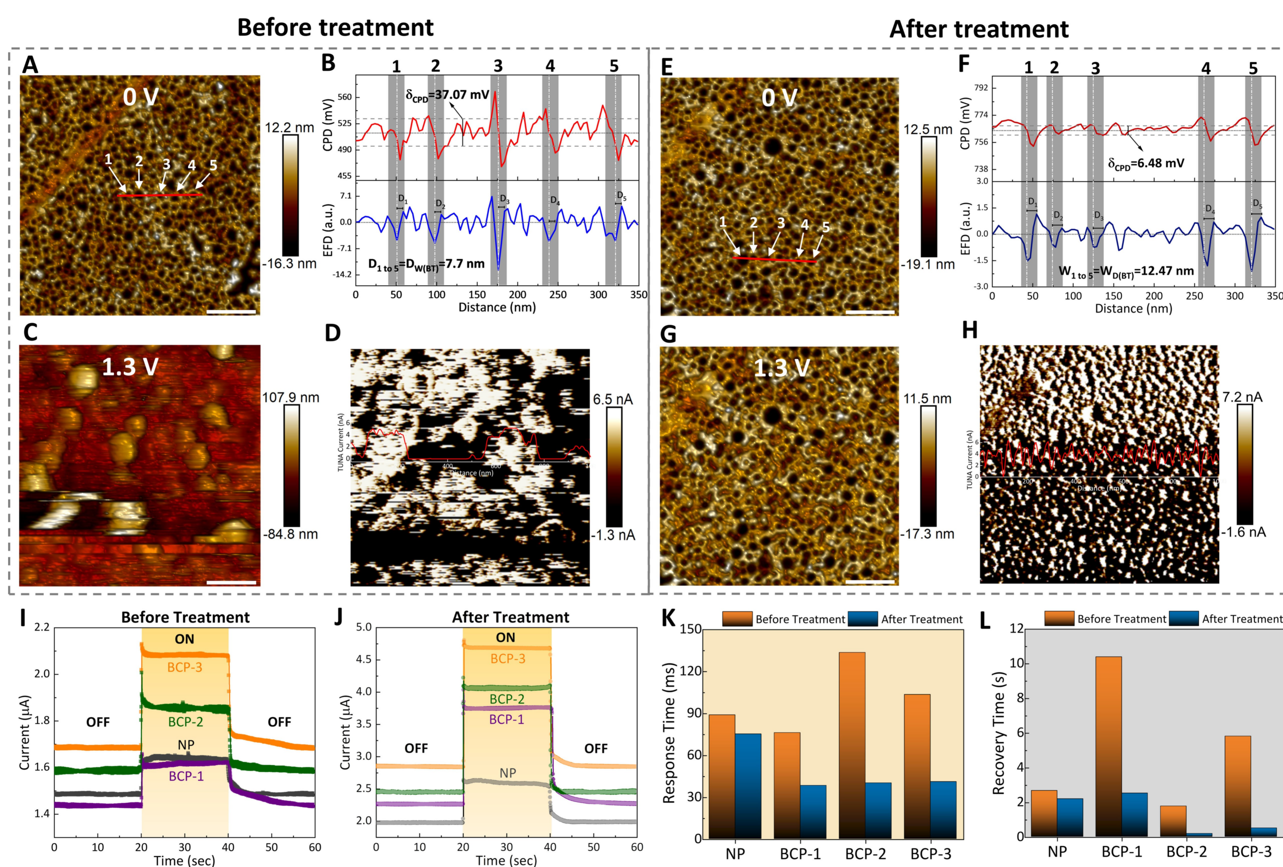

Figure 6. Atomic force microscopy (AFM) and photoelectrochemical response of samples before and after plasma treatment. Topography at applied bias voltages of A, E) 0 V and C, G) 1.3 V with D, H) equivalent current profile by PeakForce tunneling atomic force microscopy (PF-TUNA), scale bar = 200 nm. Contact potential difference (CPD) and its derivative, electrical field difference (EFD) observed from a red line of 350 nm across 5 indicated pores B) before and F) after plasma treatment. Photoelectrochemical response on samples I) before and J) after plasma treatment, with respective K) response and L) recovery time for CuTe film.

carrier transport more effective. This result supported the observation in Figures 6G and H, showing a symmetrically distributed TUNA current profile along the framework with a stable topography (Figures 6D and E).

From the acquired results at the nanoscale by C-AFM, we further investigated the photoelectrochemical responses of the pristine and plasma treated films under the experimental conditions mentioned in Supporting Information Note 6. We confirmed the transient behavior of the current with periodic switching intervals of 20 s under dark and illuminated conditions (Figures 6I and J). The values were extracted between 10 % and 90 % from acquired photoelectrochemical responses (Figures S32A, S32B, and Table S6). The samples exposed to plasma showed a tremendous improvement in the time response compared to the pristine films. The transient behavior of the plasma-treated films exhibited an improvement in the response time of 15.38 % for NP film and approximately 60.01 % for mesoporous films (Figure 6K). For the recovery time, NP samples showed only 17.95 % improvement, whereas the mesoporous films showed a significant enhancement of approximately 85.61 % compared to their counterparts before treatment (Figure 6L). The data suggested that after Ar plasma treatment, the mesoporous samples outperformed the NP film with a 4-fold improvement in transient performance. Furthermore, in the pristine films, we observed a relatively small change between the light and dark currents (Figures S32C and S32D). In contrast, the plasma-treated films showed a steady increase in the current with increasing pore diameters, among which the mesoporous samples showed an average of 15 % improvement in the dark current and 30 % improvement in the illuminated current compared to the NP film. This could be attributed to the observed nanoscopic electrical improvement in the Ar plasma-exposed mesoporous CuTe. The effective changes in the photo-to-dark current (PDC) ratio and responsivity before and after plasma treatment were examined (Figures S32E, S32F, and Supporting Information Note 7). The treated films showed better responsivity to visible light, with a higher sensitivity upon increasing the functional area of the film. The sensitivity increased in the case of long-range ordered materials and vice versa for short-range ordered materials (Tables S6 and S7). The key reason for such an enhancement in the electrical characteristics was that inert Ar plasma eliminated weakly bonded surface oxides and passivated unsaturated surface dangling bonds. This significantly reduced the surface defects in mesoporous materials with a relatively large surface area, leading to a better

© 2022 The Authors. Angewandte Chemie International Edition published by Wiley-VCH GmbH

photoconversion efficiency. Moreover, the rearranged domain structure markedly improved carrier transport, enabling near-ballistic transport (with minimum scattering centers) through the nanoscopic walls of the material.

Conclusion

We demonstrated the efficiency of low-power plasma treatment as a novel technique to improve the crystallinity of mesoporous materials. The plasma technique passivated surface states and engineered the crystallinity of strained mesoporous materials without changing the original porous nanoarchitecture. We have experimentally demonstrated a remarkable enhancement in crystallinity of approximately 70 % to 85 % after plasma exposure. The high crystalline quality obtained through the hybrid process of electrochemical deposition and post-growth Ar plasma exposure led to an 80 % increase in optoelectronic properties of the mesoporous CuTe materials. As a ubiquitous and globally available microprocessing tool, the implementation of low-power plasma holds promise for the development of high-performance nanoarchitectonics with great potential for scalable manufacturing and minimal structural damage. This makes low-power plasma a superior postprocessing technique which enables unique material properties that are barely achievable through conventional methods. The combination of bottom-up synthesis and top-down treatment presented in this work provides a new route for a wide variety of porous material systems to map distinctive possibilities structurally and electrically to improve the optoelectronic properties for versatile applications including photocatalysis, optical sensors, and photovoltaic devices.

Acknowledgements

This research was supported by the JST-ERATO Materials Space-Tectonics Project (JPMJER2003) and the Australian Research Council (ARC) support (DP200102546 and DE200100238). This research was also supported by Basic Science Research Program through the National Research Foundation of Korea (NRF) funded by the Ministry of Education (2020R1A6A3A03039037). A.A. acknowledges the support from the Australian government research training program (RTP). This work was partially performed at the Queensland node of the Australian National Fabrication Facility (ANFF-Q), a company established under the National Collaborative Research Infrastructure Strategy to provide nano- and micro-fabrication facilities for Australian researchers. The authors also acknowledge the facilities, scientific and technical assistance, of the Australian Microscopy & Microanalysis Research Facility at the Centre for Microscopy and Microanalysis, the University of Queensland and the Central Analytical Research Facility (CARF) operated by QUT's Institute for Future Environments. Open access publishing facilitated by The University of Queensland, as part of the Wiley - The University of Queensland agreement via the Council of Australian University Librarians.

Conflict of Interest

The authors declare no conflict of interest.

Data Availability Statement

Research data are not shared.

Keywords: Domain Enhancement · High Crystallinity · Mesoporous Semiconductors · Nanocrystalline · Plasma Treatment

[1] W. Li, J. Liu, D. Zhao, *Nat. Rev. Mater.* **2016**, *1*, 16023.
[2] Y. Wang, X. Bai, F. Wang, H. Qin, C. Yin, S. Kang, X. Li, Y. Zuo, L. Cui, *Sci. Rep.* **2016**, *6*, 26673.
[3] C. Wang, X. Wan, L. Duan, P. Zeng, L. Liu, D. Guo, Y. Xia, A. A. Elzatahry, Y. Xia, W. Li, *Angew. Chem. Int. Ed.* **2019**, *58*, 15863–15868; *Angew. Chem.* **2019**, *131*, 16010–16015.
[4] H. Lim, K. Kani, J. Henzie, T. Nagaura, A. S. Nugraha, M. Iqbal, Y. S. Ok, M. S. A. Hossain, Y. Bando, K. C. W. Wu, H.-J. Kim, A. E. Rowan, J. Na, Y. Yamauchi, *Nat. Protoc.* **2020**, *15*, 2980–3008.
[5] T. Nagaura, H. P. Phan, V. Malgras, T. A. Pham, H. Lim, A. Ashok, J. Kim, J. You, N. T. Nguyen, J. Na, *Angew. Chem. Int. Ed.* **2021**, *60*, 9660–9665; *Angew. Chem.* **2021**, *133*, 9746–9751.
[6] H. Wang, H. Y. Jeong, M. Imura, L. Wang, L. Radhakrishnan, N. Fujita, T. Castle, O. Terasaki, Y. Yamauchi, *J. Am. Chem. Soc.* **2011**, *133*, 14526–14529.
[7] W. Li, M. Liu, S. Feng, X. Li, J. Wang, D. Shen, Y. Li, Z. Sun, A. A. Elzatahry, H. Lu, *Mater. Horiz.* **2014**, *1*, 439–445.
[8] A. G. Slater, A. I. Cooper, *Science* **2015**, *348*, aaa8075.
[9] A. S. Nugraha, J. Na, M. S. A. Hossain, J. Lin, Y. V. Kaneti, M. Iqbal, B. Jiang, Y. Bando, T. Asahi, Y. Yamauchi, *Appl. Mater. Res.* **2020**, *18*, 100526.
[10] B. Jiang, C. Li, H. Qian, M. S. A. Hossain, V. Malgras, Y. Yamauchi, *Angew. Chem. Int. Ed.* **2017**, *56*, 7836–7841; *Angew. Chem.* **2017**, *129*, 7944–7949.
[11] C. Li, Ö. Dag, T. D. Dao, T. Nagao, Y. Sakamoto, T. Kimura, O. Terasaki, Y. Yamauchi, *Nat. Commun.* **2015**, *6*, 6608.
[12] M. Javadi, H. Torbatiyan, Y. Abdi, *Appl. Phys. Lett.* **2017**, *111*, 063113.
[13] L. Nhon, A. D. Taggart, T. Moot, M. K. Brennaman, P. Jagadesan, K. S. Schanze, J. F. Cahoon, J. R. Reynolds, *Chem. Mater.* **2020**, *32*, 8158–8168.
[14] E. J. Crossland, N. Noel, V. Sivaram, T. Leijtens, J. A. Alexander-Webber, H. J. Snaith, *Nature* **2013**, *495*, 215–219.
[15] T. Zhu, Y. Liu, T. Ding, W. Y. Fu, J. Jarman, C. X. Ren, R. V. Kumar, R. A. Oliver, *Sci. Rep.* **2017**, *7*, 45344.
[16] S. Wang, T. He, P. Chen, A. Du, K. Ostrikov, W. Huang, L. Wang, *Adv. Mater.* **2020**, *32*, 2001385.
[17] P. Yang, D. Zhao, D. I. Margolese, B. F. Chmelka, G. D. Stucky, *Nature* **1998**, *396*, 152–155.
[18] A. S. Poyraz, C.-H. Kuo, S. Biswas, C. K. King'ondu, S. L. Suib, *Nat. Commun.* **2013**, *4*, 2952.
[19] J. Choi, H.-K. Jeong, M. A. Snyder, J. A. Stoeger, R. I. Masel, M. Tsapatsis, *Science* **2009**, *325*, 590–593.

© 2022 The Authors. Angewandte Chemie International Edition published by Wiley-VCH GmbH

[20] F. Giordano, A. Abate, J. P. C. Baena, M. Saliba, T. Matsui, S. H. Im, S. M. Zakeeruddin, M. K. Nazeeruddin, A. Hagfeldt, M. Graetzel, *Nat. Commun.* **2016**, *7*, 10379.
[21] L. Tian, R. Tyburski, C. Wen, R. Sun, M. Abdellah, J. Huang, L. D'Amario, G. Boschloo, L. Hammarström, H. Tian, *J. Am. Chem. Soc.* **2020**, *142*, 18668–18678.
[22] I. Daskalakis, I. Vamvasakis, I. T. Papadas, S. Tsatsos, S. A. Choulis, S. Kennou, G. S. Armatas, *Inorg. Chem. Front.* **2020**, *7*, 4687–4700.
[23] K. Ostrikov, E. Neyts, M. Meyyappan, *Adv. Phys.* **2013**, *62*, 113–224.
[24] Y. Liu, H. Nan, X. Wu, W. Pan, W. Wang, J. Bai, W. Zhao, L. Sun, X. Wang, Z. Ni, *ACS Nano* **2013**, *7*, 4202–4209.
[25] L. Liu, Y. Zhang, W. Wang, C. Gu, X. Bai, E. Wang, *Adv. Mater.* **2011**, *23*, 1246–1251.
[26] S. Wi, H. Kim, M. Chen, H. Nam, L. J. Guo, E. Meyhofer, X. Liang, *ACS Nano* **2014**, *8*, 5270–5281.
[27] S. Xiao, P. Xiao, X. Zhang, D. Yan, X. Gu, F. Qin, Z. Ni, Z. J. Han, K. Ostrikov, *Sci. Rep.* **2016**, *6*, 19945.
[28] E. Yu, S.-C. Kim, H. J. Lee, K. H. Oh, M.-W. Moon, *Sci. Rep.* **2015**, *5*, 9362.
[29] G. S. Armatas, M. G. Kanatzidis, *Nano Lett.* **2010**, *10*, 3330–3336.
[30] G. Fanchini, A. Tagliaferro, *Appl. Phys. Lett.* **2004**, *85*, 730–732.
[31] J. J. Cardiel, H. Furusho, U. Skoglund, A. Q. Shen, *Sci. Rep.* **2015**, *5*, 17941.
[32] Y. Nie, Z. Gu, Y. Wei, T. Hao, Z. Zhou, *Polym. J.* **2017**, *49*, 309–317.
[33] Y. Hou, E. Aydin, M. D. Bastiani, C. Xiao, F. H. Isikgor, D.-J. Xue, B. Chen, H. Chen, B. Bahrami, A. H. Chowdhury, A. Johnston, S.-W. Baek, Z. Huang, M. Wei, Y. Dong, J. Troughton, R. Jalmood, A. J. Mirabelli, T. G. Allen, E. V. Kerschaver, M. I. Saidaminov, D. Baran, Q. Qiao, K. Zhu, S. D. Wolf, E. H. Sargent, *Science* **2020**, *367*, 1135–1140.
[34] J. U. Salmón-Gamboa, A. H. Barajas-Aguilar, L. I. Ruiz-Ortega, A. M. Garay-Tapia, S. J. Jiménez-Sandoval, *Sci. Rep.* **2018**, *8*, 8093.

Manuscript received: October 31, 2021
Accepted manuscript online: January 25, 2022
Version of record online: February 11, 2022

© 2022 The Authors. Angewandte Chemie International Edition published by Wiley-VCH GmbH